UV- and visible-light photocatalysis using Ni–Co bimetallic and monometallic hydrotalcite-like materials for enhanced CO_2 methanation in sabatier reaction

Rafael Canales, M. Gil-Calvo, V. Laura Barrio [*]

Bilbao School of Engineering (University of the Basque Country), Bilbao, Spain

ARTICLE INFO

ABSTRACT

The CO_2 catalytic reduction activities of four different Co-modified Ni-based catalysts derived from hydrotalcite-like materials (HTCs) prepared by co-precipitation method were investigated under thermal and photocatalytic conditions. All catalysts were tested from 473 to 723 K at 10 bar (abs). The light intensity for photocatalytic reactions was 2.4 W cm^{-2}. The samples were characterized to determine the effect of morphological and physicochemical properties of mono-bimetallic active phases on their methanation activity. The activity toward CO_2 methanation followed the next order: Ni > Co–Ni > Co. For the monometallic Ni catalyst an increase of a 72% was achieved in the photo-catalytic activity under UV and vis light irradiation at temperatures lower by > 100 K than those in a conventional reaction. Co-modified Ni based hydrotalcite catalysts performed with stability and no deactivation for the 16 h studied under visible light for methanation at 523 K due to the presence of basic sites.

1. Introduction

The prices of conventional fuels have been fluctuating worldwide depending on market supply and demand as well as climate change. Furthermore, the war in Ukraine has highlighted the necessity of transitioning from fossil fuels to green energy according to the European Union's (EU) Green Energy Deal. The European Commission proposed that EU should end its dependence on foreign countries for fossil fuels. The 2022 Intergovernmental Panel on Climate Change (IPCC) report deplored that only a few technologies are available for rapidly transitioning to a low-carbon economy. Green hydrogen has strong potential to replace fossil fuels, but its deployment remains challenging. The EU has targeted the production of 10 Mt of green H_2 (~300 TWh/y); however, the demand expected by 2050 is > 2200 TWh/y, which requires large-scale production capacity and infrastructure. One such technology is the power-to-gas (PtG) technology (Fig. 1), which produces green chemical compounds from renewable or excess electricity [1,2]. The main product is hydrogen, which can be used directly as fuel for energy or can be converted to methane, syngas, electricity, liquid fuels, or storage energy. Interestingly, this surplus energy can be used in the conversion of CO_2 to methane, which aids in the mitigation of the energy-carbon footprint.

The CO_2 methanation reaction ($CO_2 + 4H_2 \rightleftharpoons CH_4 + 2H_2O$) is an exothermic reaction favored at low temperatures [3]. Ni, Rh, Ru, Au, and Ag have been previously used as catalytic materials for CO_2 activation in both thermo- and photocatalytic reactions. The effect of different metal oxide supports (SiO_2, Al_2O_3, CeO_2, and TiO_2) on CO_2 hydrogenation depends on their surface area and oxygen

---

vacancies as well as their ability to synthesize catalysts with well-dispersed active metals and strongly basic sites [4–8].

Cobalt is one of the commonly used metals for CO_2 methanation due to the high activity and selectivity to methane due to the quick generation in the reduced cobalt sites normally at temperatures higher to 673 K. The main role of the Co^0 is to enable the fast hydrogenolysis of adsorbed intermediate species due to surface properties improvement like basicity and H_2 uptake. Paulina Summa et al. observed that 1%Co on Ni–Mg–Al hydrotalcite exhibited the best activity results with 77% of CO_2 conversion at 573 K as the reducibility of Ni species, hydrogen uptake and acidic/basic properties improved [9]. Nevertheless, CO_2 hydrogenation with CoO as the active phase is known to induce the RWGS reaction and Co^0 sites to induce methanation [10]. In Table 1, CO_2 conversion of Ni and Co based catalysts are compiled, for comparison purposes, taken into account different metal loadings, synthesis methods and temperatures with a 50 K variation from 523 to 623 K. Leilei Xu et al. reported the synergistic effect of Ni–Co active metals supported on a mesoporous Al_2O_3 with ratio of 20% (Co/Co + Ni) can enhance the Sabatier process at low temperature [11]. In the case of Chuanfei Liang et al., they stated that Co/Al_2O_3 was more active than Ni/Al_2O_3 catalysts due to the formation of different intermediates generated during the reaction [12]. For David Méndez-Mateos et al., they studied the methanation of CO_2 and the deactivation by H_2S with monometallic $13Ni/Al_2O_3$ promoted by a 4% wt. of Co. But this promoter generated a blockage of active centers decreasing the activity with respect to the monometallic [13].

Other authors studied, the different bimetallic contents: like $2Ni–8Co/SiO_2$ and $5Ni–5Co/SiO_2$ nanocomposite catalysts which exhibited high activity in the Sabatier process with a CH_4 yield of an 81–88% at 723 K. This activity enhanced was due to the Ni–Co nanoparticles acting cooperatively accumulated into the nanosilica matrix and the formation of O-intermediates bound to the bimetallic catalyst [14]. Finally, the effect of adding different promoters (Fe, Mn, Cu, …) to a bimetallic $15Ni-12.5Co/Al_2O_3$ catalyst enhanced the activity due to the increase in Ni dispersion and higher crystallinity by a certain Fe content [15].

Regarding the use of noble metals such as Au-Ni [5], Ru [16,17] and Ag–Ni [18], it has been a focus of study for photocatalytic studies due to the good results achieved, but the use of non-noble metals like Ni and Co presents a game changing technology with high interest [19,20]. Thus, catalysis of CO_2 methanation at low temperature with non-noble metals is still a major challenge. Moreover, the main aim was to compare the non-light experiments with two photocatalytic experiments for a monometallic Co-hydrotalcite, Co–Ni-hydrotalcite and Ni-hydrotalcite.

In this study, the photocatalysis of the traditional Sabatier reaction was investigated using two different light sources (UV and visible light) and the results were compared with those obtained from the conventional thermocatalytic process. Hydrotalcite-like materials containing different loadings of Co and Ni prepared via a previously reported co-precipitation method were used as the active metal catalysts. Divalent cobalt ions are replaced by divalent Ni species which results in the formation of higher crystalline phases once calcined. Hydrotalcite-like materials showed the formation of high mesoporous surface area and high basic properties enhancing activity at lower temperatures. Despite being explored for convectional CO_2 methanation [21], there are few studies focused on the use of hydrotalcites for photocatalytic Sabatier reaction. In this work, the synergistic effect of Ni and Co as active catalytic and photocatalytic centers was investigated for Sabatier reaction. Modification of Ni-based catalysts with Co will allow a more stable catalyst mainly at low temperatures.

2. Experimental section

2.1. Catalyst preparation

Hydrotalcite-like materials containing Mg, Al, and different loadings of Ni and Co were synthesized using a previously reported co-precipitation method [22]. The concentration of the active metal has been maintained in all the prepared catalysts. The metal precursors used were: $Co(NO_3)_2 \cdot 6H_2O$ (102.0% purity, Alfa Aesar, Kandel, Germany), $Ni(NO_3)_2 \cdot 6H_2O$ (99.999% purity, Sigma-Aldrich, USA), $Mg(NO_3)_2 \cdot 6H_2O$ (≥99% purity, Honeywell-Fluka, Muskegon, MI, USA), and $Al(NO_3)3 \cdot 9H_2O$ (≥98.5% purity, Merck, Darmstadt, Germany). A solution of 1 M metal salt diluted in Milli-Q water was added to a beaker. The molarity was fixed at M^{2+}/M^{3+} of 3; thus, $M^{3+}/(M^{2+}+M^{3+}) = 0.25$. The four catalysts were based on nominal metal contents listed in Table 2, substituting nickel for cobalt content.
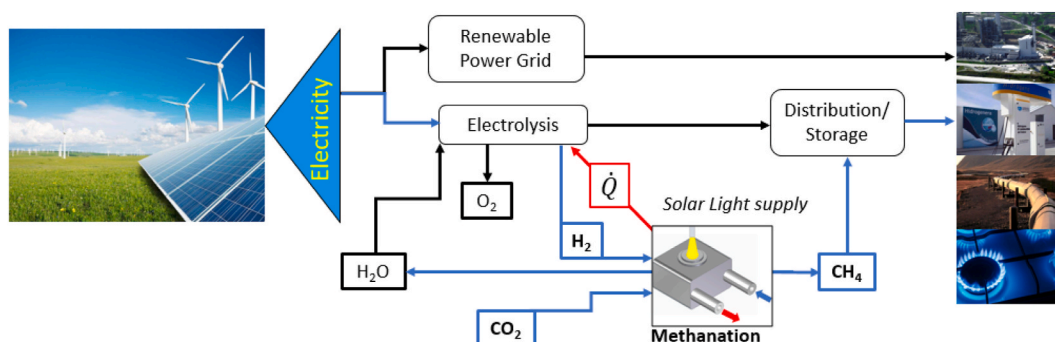

Fig. 1. Process flow diagram of Power-to-Gas (PtG) technology.

Table 1
Table of comparison with the catalytic performance using Co & Ni as active metals.

Metal precursors	CO_2 conversion (%)	T (K)	Metal content	Preparation Method	Literature (Ref. number)
Co, Ni, Al	18-62-72	523-573-623	2Co–8Ni	Evaporation induced self-assemble	[11]
Ni, Co, Al	60-80-84		15Co	Incipient impregnation	[12]
	10-25-45		15Ni		
	70-82-84		25Co		
	18-40-68		25Ni		
Ni, Co, Mg, Al	1-27-61		15Ni	Co-precipitation	[9]
	9-74-83		15Ni-0,5Co		
	24-77-89		15Ni–1Co		
	17-82-81		15Ni–2Co		
Ni, Co, Al	0-0-88		13Ni	Incipient impregnation	[13]
	0-0-0		13Ni–4Co		
Ni, Co, Si	4-36-85		10Ni	Solvate-stimulated modification	[14]
	42-81-95		10Co		
	11-42-91		5Ni–5Co		
	23-89-100		2Ni–8Co		
Ni, Co, Al	12-48-72		15Ni-12,5Co	Mechanochemical	[15]

Freshly prepared 2 M NaOH ($\geq$98% purity, Honeywell-Fluka, Muskegon, MI, USA) and 0.125 M Na_2CO_3 (99.5–100.5% purity, Panreac, Barcelona, Spain) solutions were added to the metal salt solutions to adjust their pH to 10 $\pm$ 0.2, following which the solutions were aged for 24 h. Each solution was then pressure-filtered and washed in order to remove ions (Na^+ and NO_3^-). To finish, the solid achieved was dried overnight at 373 K and afterwards calcined (773 K, 5 K/min for 5 h).

2.2. Characterization of catalysts

Inductively Coupled Plasma Optical Emission Spectroscopy (ICP-OES) in a PerkinElmer Optima 3300DV was performed. The catalysts metal contents were measured by disaggregation with aqua regia digestion at 453 K.

Textural properties. The surface area was measured using the method of the multipoint Brauner-Emmett-Teller (BET) with the N_2 adsorption data, and the pore size distribution. To remove humidity or other adsorbed gases, catalysts were first vacuum degassed (573 K for 3 h) using a Quantachrome Autosorb IQ instrument.

X-ray diffraction (XRD) patterns were obtained in a XPert Pro PANalytical diffractometer, and the crystalline phases by comparing them with the International Centre for Diffraction Data (ICDD) database. The calcined catalyst samples were analyzed in the range 2θ = 5–80° using λCuKα = 0.15418 nm.

H_2-temperature-Programmed Reduction (H_2-TPR). The catalysts reducibility was determined using an AutoChem II Instrument (Micromeritics, USA). The impurities were initially desorbed using Ar at 573 K for 1 h. Subsequently, the catalysts were subjected to 5 vol% H_2/Ar gas. The reduction profile was recorded while increasing the temperature to 1200 K at 10 K/min.

CO_2-Temperature-Programmed Desorption (CO_2-TPD) profiles were measured in a Autochem II Micromeritics instrument to analyze the basicity of the catalysts. Fifty milligrams of calcined catalyst were used for the test. The samples were degassed with He gas (flow rate: 38 mL/min for 1 h). The temperature was initially increased to 773 K at the rate of 10 K/min and then decreased to 353 K. Subsequently, the catalysts were purged with 5 vol% CO_2/He gas (flow rate: 25 mL/min for 1 h). Then, the temperature was increased to 873 K at 10 K/min with He to record the desorption curve.

UV–visible Diffuse Reflectance Spectroscopy (UV–vis DRS) technique was used to determine the optical properties and band gap of samples using a Shimadzu 3600 UV–Vis spectrophotometer. The spectra were recorded in the range 2200–200 nm.

X-ray Photoelectrons Spectroscopy (XPS) spectra were recorded to calculate the oxidation states using a SPECS system with an energy analyzer Phoibos 150 1D-DLD and an Al Kα.

Scanning Transmission Electron Microscopy-using energy dispersive X-ray Spectroscopy (STEM-EDS). This technique was used to analyze the morphology of active phases via STEM-EDS. The measurements were performed using a TECNAI G20 TWIN transmission electron microscope at 200 kV and an EDS detector (EDAX) (see Fig. 1).

Table 2
Nominal metal contents.

	Metal content (wt.%)			
	Ni	Co	Mg	*Al*
27Co	–	27	50	23
8Co–19Ni	8	19	50	23
6Co–21Ni	21	6	50	23
27Ni	27	–	50	23

2.3. Activity tests

The methanation reaction was conducted at 10 bar (abs) over a wide temperature range (473–723 K) in a commercial photoreactor. Prior to the reaction, catalytic systems were reduced based on the H_2-TPR results with a ratio of H_2 (99.999%)/N_2 (99.999%) equal to 3:1. The activities were measured in terms of CH_4 yields, CO_2 and H_2 conversions. Thus, all the catalysts were previously reduced under three different reaction conditions: 1) non-photocatalytic, 2) UV light (365 nm), and 3) visible light (470 nm). All experiments were performed at a fixed space velocity (WSHV) of 55.7 h^{-1} and for the photocatalytic experiments, the same light intensity (2.4 W/cm^2) was used. The temperature was controlled using a thermocouple located in the middle of the chamber, where the catalyst was located. Fig. 2 shows that the light penetrates to approximately 1 μm of the catalytic bed, which suggests the existence of a small temperature gradient.

3. Results & discussion

3.1. Catalysts characterization

3.1.1. Chemical and textural properties

All calcined samples exhibited type IV isotherms (Fig. S1) associated with mesoporous materials. The four hysteresis loops are attributed to networks of pores of different widths or the presence of spheroidal cavities [21]. The textural properties obtained from the BET analysis (Table 3) showed that for Ni and Co monometallic materials presented higher surface area and pore size than for the bimetallic catalysts. Pore volume was also affected by the metal substitution due to pore blockage of the material mainly for the systems with higher nickel content [11,23].

3.1.2. XRD

The XRD results for dried and calcined samples are shown in Fig. 3. All samples exhibited a hydrotalcite-like structure as expected (Fig. 3a). Thus, XRD patterns of the dried hydrotalcite-like materials (HTC) exhibited the typical pattern of layered double hydroxides or hydrotalcites. with characteristic reflections of the three basal planes identified at $2\theta = 11.4°$, $22.8°$ and $34.8°$. Moreover, other reflections associated with the non-basal planes at $2\theta = 60.7°$ and $61.8°$, respectively, were also identified (ICDD 14–191) [24]. We observed that lower Co content resulted in higher crystallinity, which indicates that Ni favors the crystallization of the hydrotalcite phase.

Calcination of the catalysts partially destroyed the typical crystalline structure of HTC-derived materials, transforming them into less-crystalline metal oxides. Metal oxides with different crystalline phases can be obtained under different calcination conditions [24, 25]. The XRD patterns in Fig. 3b suggest the existence of three phases: periclase (PDF 45–946), bunsenite (PDF 47–1049), and $AlNi_3$ (PDF 09–0097) and three different spinel phases: $MgAl_2O_4$ (PDF 21–1152), Co_3O_4 (PDF 42–1467), $CoAl_2O_4$ (PDF 44–160), and $NiAl_2O_4$ (PDF 10–339). For catalysts with lower Co contents, higher crystallinity was observed for the NiO and $AlNi_3$ species formed [26].

3.1.3. H_2-temperture Programmed Reduction

The H_2-TPR profiles of the catalysts after calcination are compiled in Fig. 4. Two different regions, high temperature (HT) and low temperature (LT), were observed. The high-temperature peaks are attributed to the reduction of Co and Ni oxides to NiO–MgO and NiO–Al_2O_3 solid solutions, which are stable and difficult to reduce [27]. However, Ni–Co bimetallic systems exhibited low-temperature peaks, suggesting that the presence of both metals promotes the reducibility of mixed oxides. The smaller peak in the low-temperature region from 500 to 600 K is attributed to Co_3O_4, CoO, and NiO species with weak interactions [28,29].
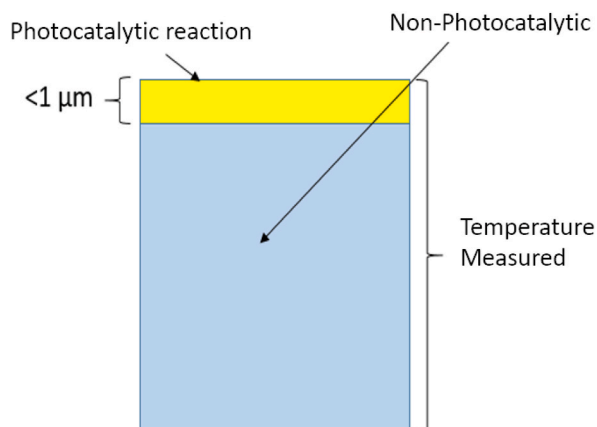

Fig. 2. Schematic of the catalytic bed.

Table 3
Elemental composition obtained from ICP-OES and textural properties.

Catalyst	Elemental composition (wt.%)	Surface area ($m^2 \cdot g^{-1}$)	Pore volume ($cm^3 \cdot g^{-1}$)	Pore size (nm)
27Co	27.0 (Co) 51.7 (Mg) 21.3 (Al)	166.3	0.21	5.5
19Co–8Ni	18.7 (Co) 8.0 (Ni) 52.4 (Mg) 20.9 (Al)	142.3	0.21	3.0
6Co–21Ni	6.1 (Co) 19.8 (Ni) 53.3 (Mg) 20.8 (Al)	159.0	0.33	4.2
27Ni	26.2(Ni) 52.6 (Mg) 21.2 (Al)	177.0	0.50	5.4
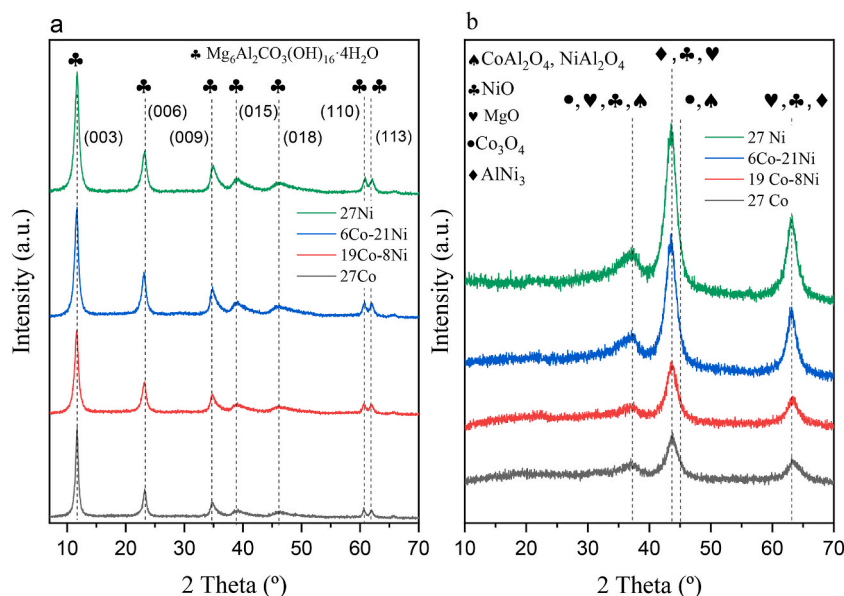
Fig. 3. XRD patterns of: a) dried catalysts and b) calcined catalysts at 773 K.
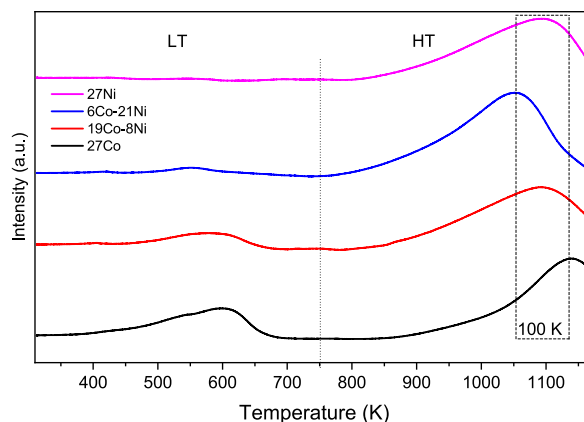

Fig. 4. Reduction profiles for calcined hydrotalcite-derived materials.

3.1.4. CO₂-temperature programmed desorption

The CO_2-TPD profiles of the calcined samples are depicted in Fig. 5. As it can be observed, CO_2 desorption peaks appeared in the range of 353–873 K according to the different types of basic sites. The desorption peak at 423 K indicates the presence of weak Brønsted sites. The desorption band in the region 473–623 K was ascribed to the basic sites with medium-strength crucial for methanation, whereas the peak at high temperatures (673–723 K) was ascribed to basic sites with strong strength [12,23,30]. The relative total area of these peaks indicated that the strength of the basic sites decreased in the following order as shown in Table 4: Ni HTC catalyst > Co–Ni HTC catalyst > Co HTC catalyst. Thus, the amount of basic sites in the monometallic Ni catalyst was higher than that for the monometallic Co sample. Moreover, the strength of the weakly basic sites was slightly lower in the bimetallic catalysts. Thus, for 27Ni and 6Co–21Ni, the higher number of medium-strength active species could result in a stronger interaction between CO_2 and these basic
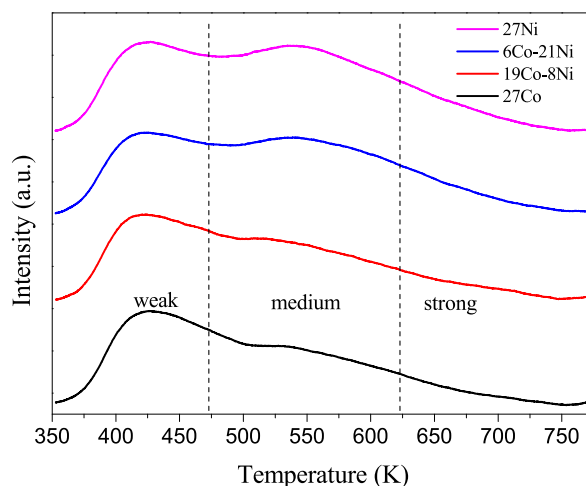
Fig. 5. CO_2-TPD profiles of the calcined hydrotalcite-derived materials.

Table 4
Basic sites for the calcined hydrotalcite-like materials (HTCs).

Sample	Weak	Medium	Strong	mmol CO_2/g adsorbed
27Co	32.4%	40.4%	27.2%	0.28
19Co–8Ni	30.8%	42.5%	26.7%	0.26
6Co–21Ni	25.5%	46.1%	28.4%	0.30
27Ni	25.8%	46.4%	27.8%	0.34

sites.

3.1.5. UV–vis DRS

The DRS spectra of the calcined samples are presented in Fig. 6. Broad absorption bands appeared for all the systems. In the case of the Co systems, Co^{2+} and Co^{3+} cations appeared at 600–700 nm and 330–480 nm, respectively [31–33]. This suggests that a part of the Co^{2+} cations were oxidized to Co^{3+} during the calcination step. In the case of the Ni systems, the spectra showed intense signals in the UV region. The first peak was at ~200–300 nm, which is related to the $O^{2-} \rightarrow Ni^{2+}$ charge transfer, and a second peak at ~400 nm that
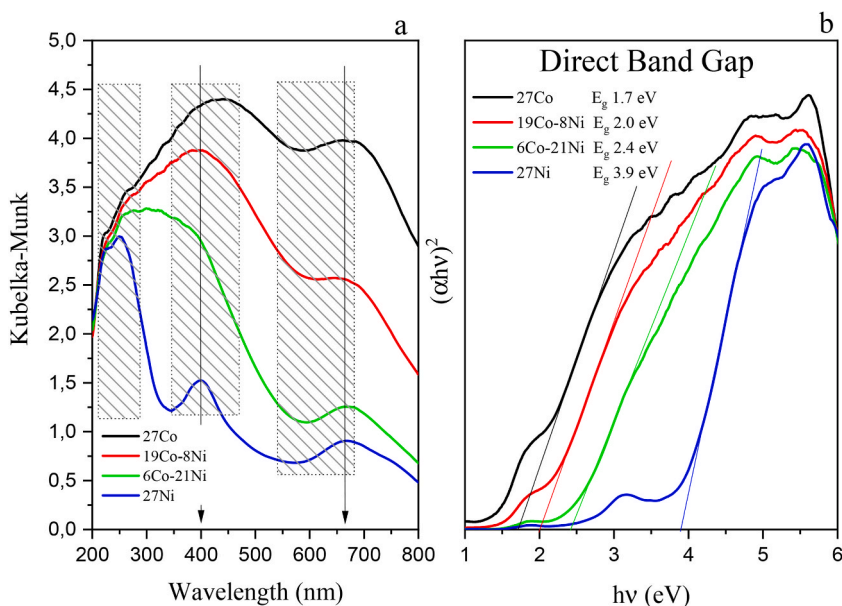

Fig. 6. a) UV–vis DRS spectra of calcined samples and b) direct band gap obtained from K-M absorbance spectra.

can be attributed to Ni^{2+} species, mainly in the octahedral coordination, implying the formation of $NiAl_2O_4$-like surface spinels [34]. Finally, the band located at 670 nm was attributed to tetrahedral Ni^{2+} ions.

Furthermore, overlapping absorption ranges were observed for some species, which make it difficult to clearly identify the formed species. However, for bimetallic catalysts, the wide band at 330–480 nm suggests that most of the Ni^{2+} species are octahedrally coordinated [34].

The direct bandgap was estimated by applying the Tauc equation and plotting $(\alpha h\nu)^2$ vs. $(h\nu)$. This complementary analysis revealed that the bimetallic samples shifted to a lower energy (red shift), which could be attributed to the interaction of the Ni 3d
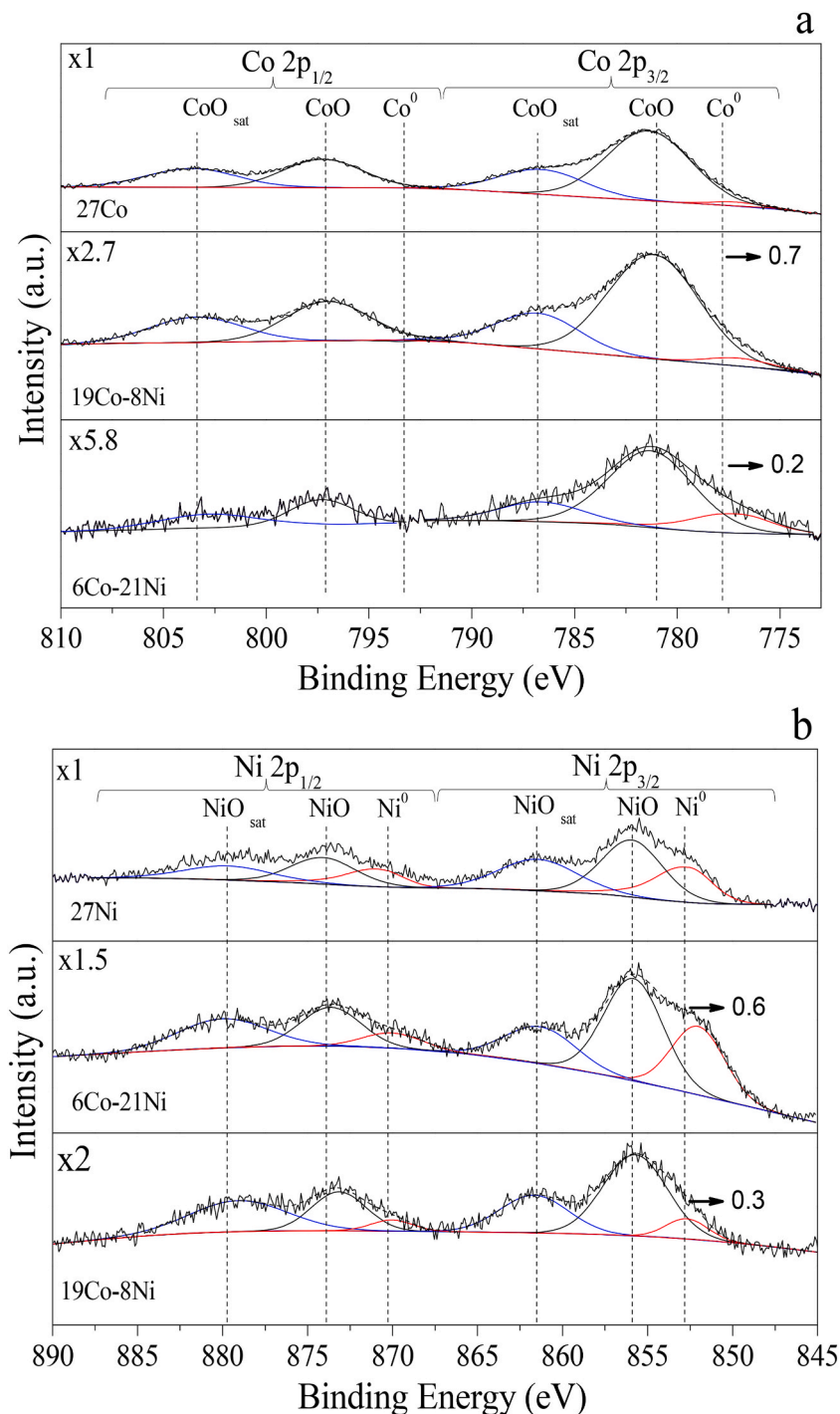

Fig. 7. XPS spectra of the reduced hydrotalcite-derived catalysts a) Co $2p_{3/2}$ and $2p_{1/2}$ and b) Ni $2p_{3/2}$ and $2p_{1/2}$.

electrons and O 2p core holes at the valence and conduction bands [35].

This complementary analysis reveals that the band of the monometallic Co sample exhibited a higher absorption maximum range, which could indicate the incorporation of a significant amount of Co in the matrix.

3.1.6. XPS

The chemical states of Co and Ni were identified using XPS analysis. The deconvoluted profiles of the XPS spectra of the reduced catalysts are presented in Fig. 7. For the Co XPS profiles of the catalysts, three peaks were observed at 778.3, 781.0, and 786.8 eV.

In the monometallic Co sample, the peak at 778.3 eV corresponds to metallic cobalt. In the case of the bimetallic samples, this peak appears at lower binding energies but for all the samples the peak contribution is very low. The peak at 781.0 eV is assigned to spinel species like CoO with the satellite peak with a difference of 5.7 eV [36–38]. For the bimetallic samples, this peak shifted to lower binding energies due to the formation of new oxygen species interacting with the support according to H_2-TPR results.

The binding energies of the $Ni2p_{3/2}$ signal for the monometallic 27Ni catalyst appear at 852.9, 856.0 and 861.4 eV, corresponding to metallic Ni^0, NiO, and a satellite line, respectively, indicating the presence of $NiAl_2O_4$ spinel species [11,39]. In the case of the bimetallic catalysts, the presence of metallic Ni^0 was observed in all cases. A shift to lower binding energy of 0.3–0.6 eV was observed. Moreover, Ni and also Co reduction seems to be higher for the 6Co–21Ni catalyst.

3.1.7. STEM-EDS

Fig. 8 shows the STEM-EDS images of 27Co, 19Co–8Ni, 6Co–21Ni, and 27Ni catalysts. Highly porous metal oxide structures of the HTC-like precursors were observed, which were attributed to the co-precipitation method used for the catalyst preparation. Moreover, active metal nanoparticles (NPs) were evenly dispersed on the catalyst surface with comparable particle sizes (13 nm) and a metal dispersion of 8% for all the catalysts. In the case of Co samples, high temperature is required for the reduction of the Co species which makes the quantification of the particles challenging. In addition, strong metal-support interaction can contribute to particle sintering [40].

3.2. Catalyst performance

The performances of all the catalysts were initially analyzed in the absence of a light source (Fig. 9). The catalytic performance was measured in terms of CO_2 conversion and CH_4 yield. All catalysts exhibited high activities albeit different conversions at 650 K. Under the reaction conditions, both the active metals in the 27Ni, 6Co–21Ni, and 27Co catalysts were reduced, whereas Co was partially reduced and consistent with the XPS results.

27Ni catalyst showed higher activity than that of the unpromoted HTC 27Co over the entire temperature range. Maximum CO_2 conversion and CH_4 yield (82 and 80%, respectively) were obtained at 673 K for the 27Ni catalyst. A similar result was observed for the bimetallic 6Co–21Ni catalyst. Considering the CO_2-TPD results, we inferred that a higher Ni content increases the amount of basic sites with medium-strength, which may be responsible for the improvement in catalytic performance.

The performances of all the catalysts in the presence of UV-led photon energy are shown in Fig. 10. The activity curve shifted to lower temperatures as all the catalysts exhibited significant activity from 550 K. 27Ni and 6Co–21Ni exhibited similar CO_2 conversion and CH_4 yields under UV light irradiation with a slightly higher conversion for the 6Co–21Ni catalyst. Thus, these reaction conditions retain the same catalytic activity (73% CO_2 conversion) as that observed in the thermocatalytic experiments but at lower temperatures (641–574 K). This improvement could be ascribed to the presence of plasmonic hot electrons that are then available for the CO_2 reaction intermediates and transfer from metal NPs [18,41]. In this case, Ni, Co, or bimetallic Ni–Co NPs not only act as light absorbers and reservoirs of photogenerated electrons but also as cocatalysts by transferring electrons to CO_2 and lowering the recombination rates [42–44].

Next, we conducted catalytic experiments under **visible**-light illumination using a blue LED (470 nm) (Fig. 11) with the same photon flux as that in the UV LED. In this case, the catalytic activity was observed at even lower temperatures (500 K) than those observed for the UV-irradiation conditions. Moreover, similar to the results of the UV experiments, 27Ni and 6Co–21Ni catalysts demonstrated the same behavior with high catalytic performances with a slightly higher conversion for the 27Ni catalyst. However, the CO_2 conversion observed in this case was higher and was achieved at lower temperatures than that observed in the UV experiments; for example, a CO_2 conversion of 73% was achieved at 528 K. This indicates that the energy required for the electronic excitation was comparable in both cases even though UV light has lower wavelength and higher energy than that of visible light, generating less photons and electron movement.

Finally, the stability of 27 Ni and 6Co–21Ni catalyst for 16 h under visible light in the Sabatier reaction was investigated. As shown in Fig. 12, excellent CO_2 conversion was observed without any significant diminution.

4. Conclusions

In this study, we investigated the performances of several catalysts (monometallic Ni and Co and bimetallic Ni–Co) derived from hydrotalcite-type precursors in the Sabatier reaction with and without light irradiation. The catalysts were prepared by partially replacing Co with Ni using a co-precipitation method. Catalytic activity under UV- and visible-light illumination was higher than that observed under thermal conditions; moreover, high activity was achieved at much lower temperatures. Even though the same irradiance was used for both photoactivity tests, the higher wavelengths of visible light facilitated a higher activity owing to the higher photon flux generated. A CO_2 conversion of 73% was achieved under UV light at lower temperatures (a decrease of 67 K) than that
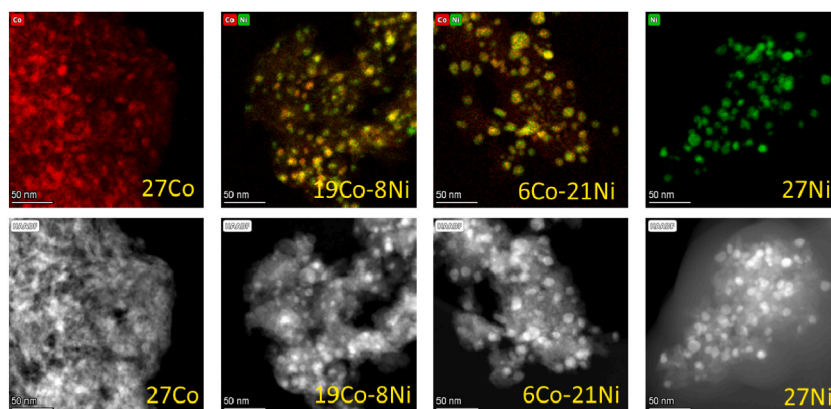
Fig. 8. STEM-EDS images of 27Co (Up: Co and Down: HAADF), 19Co–8Ni (Up: Co and Ni and Down: HAADF), 6Co–21Ni (Up: Co and Ni and Down: HAADF), and 27Ni catalysts (Up: Ni and Down: HAADF).
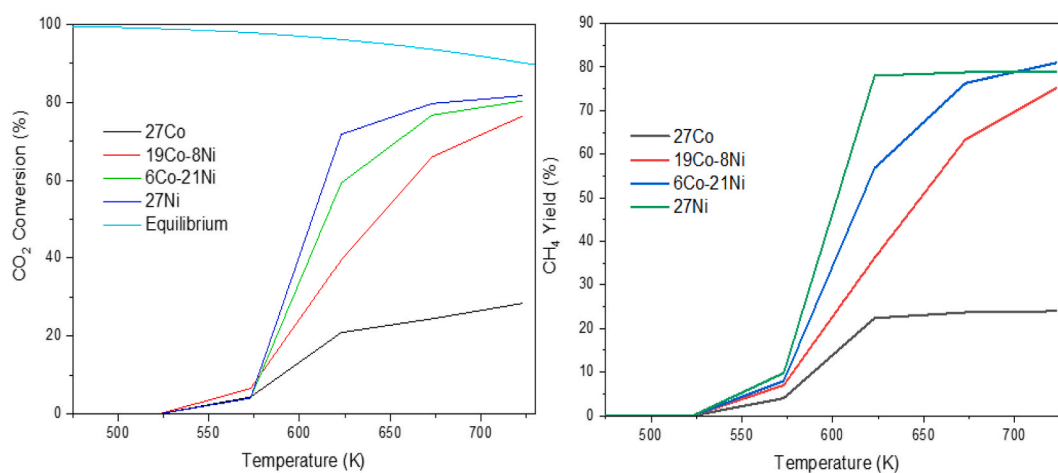

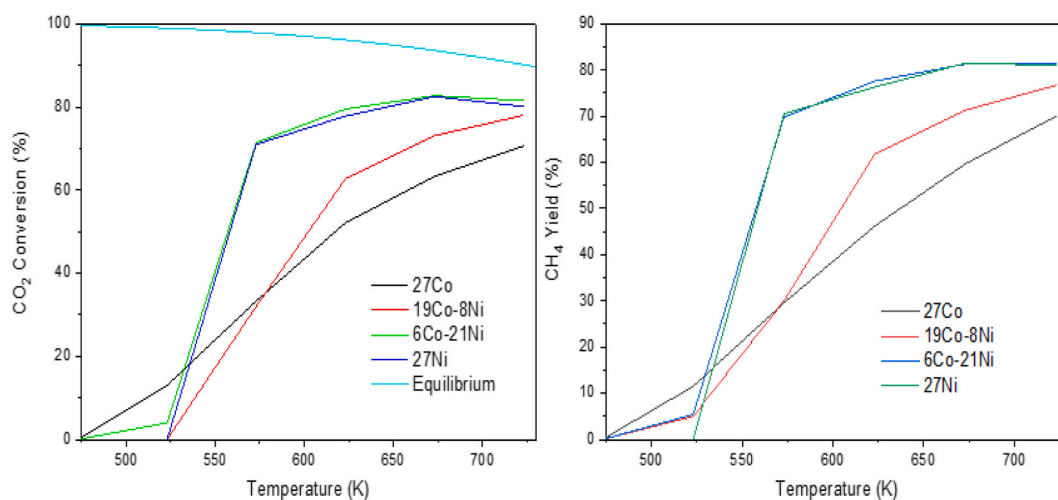**Fig. 9.** CO_2 conversion (left) and CH_4 yields (right) under thermal conditions.

Fig. 10. CO_2 conversion (left) and CH_4 yield (right) under UV light irradiation.
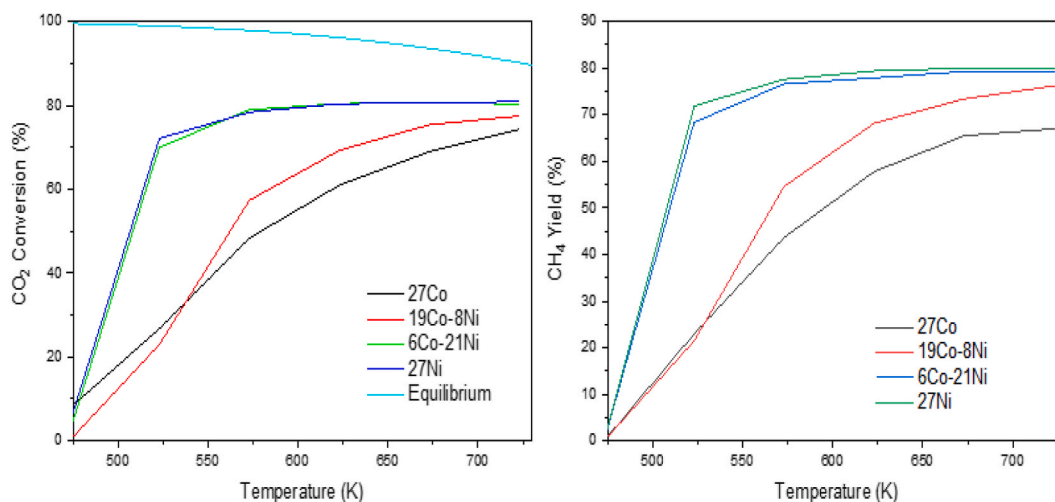
Fig. 11. CO_2 conversion (left) and CH_4 yield (right) under visible-light irradiation.
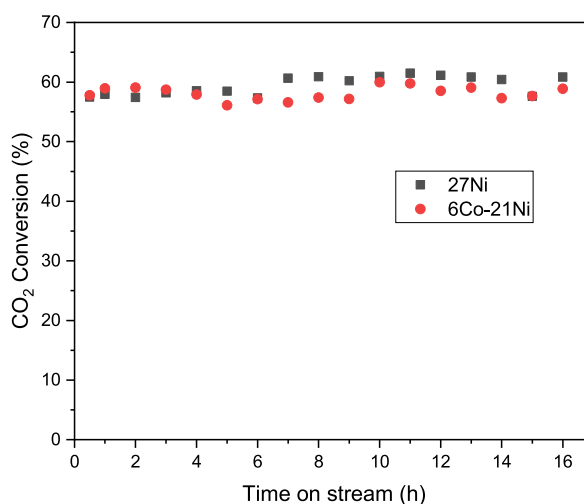

Fig. 12. Photocatalytic stability tests for 27Ni and 6Co–21Ni catalysts in CO_2 methanation at 523 K.

required in the absence of light. The best results were achieved under visible light for the 6Co–21Ni and 27Ni catalysts, where a CO_2 conversion of 73% was observed at 528 K with a slightly higher conversion for the 27Ni catalyst. Thus, the Co addition did not improve the methanation performance. The results of H_2-TPR and XRD analyses indicate that higher amounts of active Ni species and *higher catalytic* activity can be attributed to the higher *crystallinity of the catalysts*. The greater amount of Ni facilitated the formation of medium-strength basic sites, which may be responsible for the higher methanation activity achieved at lower temperatures.

For Co catalysts derived from hydrotalcite-type precursors, a high Co content did not improve thermal or/and photocatalytic activity. The divalent and trivalent Co cations in periclase and spinel-type mixed oxides, which have been identified by XRD and XPS analyses, did not activate CO_2 hydrogenation.

The hydrotalcite-derived materials prepared via the co-precipitation method improved the photocatalytic and non-photocatalytic activity by enhancing the rate of electron transfer for CO_2 hydrogenation. This preparation method could be used to replace different metals to finetune the catalytic activity of various catalysts in the future.

Author contribution statement

Rafael Canales: Conceived and designed the experiments; Performed the experiments; Analyzed and interpreted the data; Contributed reagents, materials, analysis tools or data; Wrote the paper.

Miryam Gil-Calvo: Analyzed and interpreted the data; Contributed reagents, materials, analysis tools or data.

V. Laura Barrio: Conceived and designed the experiments; Analyzed and interpreted the data; Wrote the paper.

Data availability statement

Data will be made available on request.

Declaration of competing interest

The authors declare that they have no known competing financial interests or personal relationships that could have appeared to influence the work reported in this paper.

Acknowledgements

Abbreviation

HTCs   Hydrotalcite-derived materials.

Appendix A. Supplementary data

Supplementary data to this article can be found online at https://doi.org/10.1016/j.heliyon.2023.e18456.

References

[1] R. de Richter, T. Ming, P. Davies, W. Liu, S. Caillol, Removal of non-CO_2 greenhouse gases by large-scale atmospheric solar photocatalysis, Prog. Energy Combust. Sci. 60 (2017) 68–96, https://doi.org/10.1016/j.pecs.2017.01.001.

[2] A.B.T. Nelabhotla, D. Pant, C. Dinamarca, Power-to-gas for Methanation, 2021, https://doi.org/10.1016/B978-0-12-822808-1.00008-8, 2. INC.

[3] I. Agirre, E. Acha, J.F. Cambra, V.L. Barrio, Water sorption enhanced CO_2 methanation process: optimization of reaction conditions and study of various sorbents, Chem. Eng. Sci. 237 (2021), https://doi.org/10.1016/j.ces.2021.116546.

[4] Y. Yang, J. Liu, F. Liu, D. Wu, Reaction mechanism of CO_2 methanation over Rh/TiO_2 catalyst, Fuel 276 (2020), 118093, https://doi.org/10.1016/j.fuel.2020.118093.

[5] J.N.G. Stanley, I. García-García, T. Perfrement, E.C. Lovell, T.W. Schmidt, J. Scott, et al., Plasmonic effects on CO_2 reduction over bimetallic Ni-Au catalysts, Chem. Eng. Sci. 194 (2019) 94–104, https://doi.org/10.1016/j.ces.2018.04.003.

[6] L. Truong-Phuoc, J.M. Nhut, S. Sall, G. Tuci, A. Rossin, V. Papaefthimiou, et al., Not just another methanation catalyst: depleted uranium meets nickel for a high-performing process under autothermal regime, ChemSusChem (2022), https://doi.org/10.1002/cssc.202201859.

[7] S. Tada, T. Shimizu, H. Kameyama, T. Haneda, R. Kikuchi, Ni/CeO_2 catalysts with high CO_2 methanation activity and high CH4 selectivity at low temperatures, Int. J. Hydrogen Energy 37 (2012) 5527–5531, https://doi.org/10.1016/j.ijhydene.2011.12.122.

[8] P. Riani, I. Valsamakis, T. Cavattoni, V. Sanchez Escribano, G. Busca, G. Garbarino, Ni/SiO_2-Al_2O_3 catalysts for CO2 methanation: effect of La2O3 addition, Appl. Catal. B Environ. 284 (2021), https://doi.org/10.1016/j.apcatb.2020.119697.

[9] P. Summa, K. Świrk, Y. Wang, B. Samojeden, M. Rønning, C. Hu, et al., Effect of cobalt promotion on hydrotalcite-derived nickel catalyst for CO_2 methanation, Appl. Mater. Today 25 (2021), 101211, https://doi.org/10.1016/j.apmt.2021.101211.

[10] M. Wang, G. Zhang, J. Zhu, W. Li, J. Wang, K. Bian, et al., Unraveling the tunable selectivity on cobalt oxide and metallic cobalt sites for CO_2 hydrogenation, Chem. Eng. J. 446 (2022), 137217, https://doi.org/10.1016/j.cej.2022.137217.

[11] L. Xu, X. Lian, M. Chen, Y. Cui, F. Wang, W. Li, et al., CO_2 methanation over Co–Ni bimetal-doped ordered mesoporous Al_2O_3 catalysts with enhanced low-temperature activities, Int. J. Hydrogen Energy 43 (2018) 17172–17184, https://doi.org/10.1016/j.ijhydene.2018.07.106.

[12] C. Liang, H. Tian, G. Gao, S. Zhang, Q. Liu, D. Dong, et al., Methanation of CO_2 over alumina supported nickel or cobalt catalysts: effects of the coordination between metal and support on formation of the reaction intermediates, Int. J. Hydrogen Energy 45 (2020) 531–543, https://doi.org/10.1016/j.ijhydene.2019.10.195.

[13] D. Méndez-Mateos, V.L. Barrio, J.M. Requies, J.F. Cambra, A study of deactivation by H_2S and regeneration of a Ni catalyst supported on Al_2O_3, during methanation of CO_2. Effect of the promoters Co, Cr, Fe and Mo, RSC Adv. 10 (2020) 16551–16564, https://doi.org/10.1039/d0ra00882f.

[14] A.G. Dyachenko, O.V. Ischenko, O.V. Goncharuk, M.V. Borysenko, O.V. Mischanchuk, V.M. Gun'ko, et al., Preparation and characterization of Ni–Co/SiO_2 nanocomposite catalysts for CO_2 methanation, Appl. Nanosci. 12 (2022) 349–359, https://doi.org/10.1007/s13204-020-01650-1.

[15] P. Shafiee, S.M. Alavi, M. Rezaei, F. Jokar, Promoted Ni–Co–Al_2O_3 nanostructured catalysts for CO_2 methanation, Int. J. Hydrogen Energy 47 (2022) 2399–2411, https://doi.org/10.1016/j.ijhydene.2021.10.197.

[16] P. Zhang, X. Sui, Y. Wang, Z. Wang, J. Zhao, N. Wen, et al., Surface Ru-H bipyridine complexes-grafted TiO_2 nanohybrids for efficient photocatalytic CO_2 methanation, J. Am. Chem. Soc. 145 (10) (2023) 5769–5777, https://doi.org/10.1021/jacs.2c12632.

[17] Y. Chen, J. Long, Z. Li, Efficient photothermal CO_2 methanation over RuO_2/$SrTiO_3$, Trends Chem 1 (2019) 459–460, https://doi.org/10.1016/j.trechm.2019.06.005.

[18] I. García-García, E.C. Lovell, R.J. Wong, V.L. Barrio, J. Scott, J.F. Cambra, et al., Silver-based plasmonic catalysts for carbon dioxide reduction, ACS Sustain. Chem. Eng. 8 (2020) 1879–1887, https://doi.org/10.1021/acssuschemeng.9b06146.

[19] D. Méndez-Mateos, V.L. Barrio, J.M. Requies, M. Gil-Calvo, Graphene-based versus alumina supports on CO_2 methanation using lanthanum-promoted nickel catalysts, Environ. Sci. Pollut. Res. (2023), https://doi.org/10.1007/s11356-023-26324-7.

[20] W.Y. Lim, G.W. Ho, Nickel-cobalt layered double hydroxides for photocatalytic degradation under visible light irradiation, Procedia Eng. 215 (2017) 163–170, https://doi.org/10.1016/j.proeng.2017.11.005.

[21] X. Wang, T. Zhen, C. Yu, Application of Ni–Al-hydrotalcite-derived catalyst modified with Fe or Mg in CO2 methanation, Appl. Petrochemical Res. 6 (2016) 217–223, https://doi.org/10.1007/s13203-016-0154-1.

[22] C. García-Sancho, R. Guil-López, L. Pascual, P. Maireles-Torres, R.M. Navarro, J.L.G. Fierro, Optimization of nickel loading of mixed oxide catalyst ex-hydrotalcite for H_2 production by methane decomposition, Appl. Catal. Gen. 548 (2017) 71–82, https://doi.org/10.1016/j.apcata.2017.07.038.

[23] J. Liu, K. Wu, Z. Li, W. Li, Y. Ning, W. Wang, et al., Preparation of bimetal Co–Ni supported on Mg–Al oxide for chemocatalytic upgrading of tailored fermentation products to energy intensive fuels, Green Energy Environ. (2021), https://doi.org/10.1016/j.gee.2020.10.011.

[24] R.M. Navarro, M.A. Pen, J.L.G. Fierro, Hydrogen Production by Oxidative Ethanol Reforming on Co , Ni and Cu Ex -hydrotalcite Catalysts, 2010, https://doi.org/10.1016/j.ijhydene.2010.10.084, 6.

[25] D.A. Links, RSC Advances Cobalt Hydrotalcite for the Steam Reforming of Ethanol with Scarce Carbon Production, 2012, pp. 2946–2956, https://doi.org/10.1039/c2ra00936f.

[26] G. Zhang, Y. Wang, X. Li, Y. Bai, L. Zheng, L. Wu, et al., Effect of Gd Promoter on the Structure and Catalytic Performance of Mesoporous Ni/Al$_2$O$_3$−CeO$_2$ in Dry Reforming of Methane, 2018, https://doi.org/10.1021/acs.iecr.8b03612.

[27] C. Tanios, S. Bsaibes, C. Gennequin, M. Labaki, F. Cazier, S. Billet, et al., Syngas production by the CO$_2$ reforming of CH4 over Ni–Co–Mg–Al catalysts obtained from hydrotalcite precursors, Int. J. Hydrogen Energy 42 (2017) 12818–12828, https://doi.org/10.1016/j.ijhydene.2017.01.120.

[28] Y. Guo, J. Lu, Q. Liu, X. Bai, L. Gao, W. Tu, et al., Carbon dioxide reforming of methane over cobalt catalysts supported on hydrotalcite and metal oxides, Catal. Commun. 116 (2018) 81–84, https://doi.org/10.1016/j.catcom.2018.08.017.

[29] M. Muñoz, S. Moreno, R. Molina, The effect of the absence of Ni, Co, and Ni-Co catalyst pretreatment on catalytic activity for hydrogen production via oxidative steam reforming of ethanol, Int. J. Hydrogen Energy 39 (2014) 10074–10089, https://doi.org/10.1016/j.ijhydene.2014.04.131.

[30] P. Summa, B. Samojeden, M. Motak, D. Wierzbicki, I. Alxneit, K. Swierczek, et al., Investigation of Cu promotion effect on hydrotalcite-based nickel catalyst for CO$_2$, Methanation 386 (2022) 133–145, https://doi.org/10.1016/j.cattod.2021.05.004.

[31] L.G.A. van de Water, G.L. Bezemer, J.A. Bergwerff, M. Versluijs-Helder, B.M. Weckhuysen, K.P. de Jong, Spatially resolved UV-vis microspectroscopy on the preparation of alumina-supported Co Fischer-Tropsch catalysts: linking activity to Co distribution and speciation, J. Catal. 242 (2006) 287–298, https://doi.org/10.1016/j.jcat.2006.06.004.

[32] S. Basag, F. Kovanda, Z. Piwowarska, A. Kowalczyk, K. Pamin, L. Chmielarz, Hydrotalcite-derived Co-containing mixed metal oxide catalysts for methanol incineration : role of cobalt content, Mg/Al ratio and calcination temperature, J. Therm. Anal. Calorim. 129 (2017) 1301–1311, https://doi.org/10.1007/s10973-017-6348-7.

[33] J.L. Contreras, A. Figueroa, B. Zeifert, J. Salmones, G.A. Fuentes, T. Vázquez, et al., Production of hydrogen by ethanol steam reforming using Ni–Co-ex-hydrotalcite catalysts stabilized with tungsten oxides, Int. J. Hydrogen Energy 46 (2021) 6474–6493, https://doi.org/10.1016/j.ijhydene.2020.11.143.

[34] Q.L.M. Ha, U. Armbruster, H. Atia, M. Schneider, H. Lund, G. Agostini, et al., Development of active and stable low nickel content catalysts for dry reforming of methane, Catalysts 7 (2017), https://doi.org/10.3390/catal7050157.

[35] S. Kumar, A.K. Ojha, Ni, Co and Ni-Co codoping induced modification in shape, optical band gap and enhanced photocatalytic activity of CeO$_2$ nanostructures for photodegradation of methylene blue dye under visible light irradiation, RSC Adv. 6 (2016) 8651–8660, https://doi.org/10.1039/c5ra14184b.

[36] C. Huck-Iriart, L. Soler, A. Casanovas, C. Marini, J. Prat, J. Llorca, et al., Unraveling the chemical state of cobalt in Co-based catalysts during ethanol steam reforming: an in situ study by near ambient pressure XPS and XANES, ACS Catal. 8 (2018) 9625–9636, https://doi.org/10.1021/acscatal.8b02666.

[37] NIST X-ray Photoelectron Spectroscopy Database, NIST Standard Reference Database Number 20, National Institute of Standards and Technology, Gaithersburg MD, 2000, 20899, https://doi.org/10.18434/T4T88K.

[38] A.A. Khassin, T.M. Yurieva, V.V. Kaichev, Bukhtiyarov VI, Budneva AA, Paukshtis EA, et al. Metal-support interactions in cobalt-aluminum co-precipitated catalysts: XPS and CO adsorption studies, J. Mol. Catal. Chem. 175 (2001) 189–204, https://doi.org/10.1016/S1381-1169(01)00216-3.

[39] X. Zhang, J. Wang, G. Zhang, J. Liu, ScienceDirect Co e Ni/WC-AC catalysts for dry reforming of methane : the role of Ni species, Int. J. Hydrogen Energy (2023), https://doi.org/10.1016/j.ijhydene.2022.12.360.

[40] C. Wan, K. Song, J. Pan, M. Huang, R. Luo, D. Li, et al., Ni–Fe/Mg(Al)O alloy catalyst for carbon dioxide reforming of methane: influence of reduction temperature and Ni–Fe alloying on coking, Int. J. Hydrogen Energy 45 (2020) 33574–33585, https://doi.org/10.1016/j.ijhydene.2020.09.129.

[41] X. Zhang, X. Li, D. Zhang, N.Q. Su, W. Yang, H.O. Everitt, et al., Product selectivity in plasmonic photocatalysis for carbon dioxide hydrogenation, Nat. Commun. 8 (2017) 1–9, https://doi.org/10.1038/ncomms14542.

[42] Braik M, Sow I, Nelayah J, Belkhir A, Faustini M, Mercone S, et al. Nanoscale 2021:2639–2647. https://doi.org/10.1039/d0nr06966c.

[43] Y. Liu, Z. Wang, W. Fan, Z. Geng, L. Feng, Enhancement of the photocatalytic performance of Ni-loaded TiO$_2$ photocatalyst under sunlight, Ceram. Int. 40 (2014) 3887–3893, https://doi.org/10.1016/j.ceramint.2013.08.030.

[44] S. He, J. Huang, J.L. Goodsell, A. Angerhofer, W.D. Wei, Plasmonic nickel–TiO$_2$ heterostructures for visible-light-driven photochemical reactions, Angew. Chem. Int. Ed. 58 (2019) 6038–6041, https://doi.org/10.1002/anie.201901987.